Portable NMR for quantification of breast density *in vivo*:
Proof-of-concept measurements and comparison with quantitative MRI

Nicholas D. McKay-Parry[^,1], Tony Blick[^,2, 3], Satcha Foongkajornkiat[4], Thomas Lloyd[5],

Erik W. Thompson[2,3], Honor J. Hugo[2,3,6,7] and Konstantin I. Momot[4]*

[1] Department of Medical Imaging, Gold Coast University Hospital, Southport, QLD 4215, Australia

[2] School of Biomedical Sciences, Queensland University of Technology (QUT), Brisbane, QLD 4006, Australia

[3] Translational Research Institute, Woolloongabba, QLD 4102, Australia

[4] School of Chemistry and Physics, Queensland University of Technology (QUT), Brisbane, QLD 4001, Australia

[5] Department of Radiology, The Princess Alexandra Hospital, Woolloongabba, QLD 4102, Australia

[6] School of Health and Behavioural Sciences, University of the Sunshine Coast, Sippy Downs, QLD 4556, Australia

[7] School of Medicine and Dentistry, Griffith University, Birtinya, QLD 4575, Australia

^ = Equal first authors

* Corresponding author:
Dr. Konstantin I. Momot
School of Chemistry and Physics
Queensland University of Technology (QUT)
GPO Box 2434, QLD 4001, Brisbane, Australia
Phone: +61-7-3138-1173
Email: k.momot@qut.edu.au

Abstract

Mammographic Density (MD) is the degree of radio-opacity of the breast in an X-ray mammogram. It is determined by the Fibroglandular : Adipose tissue ratio. MD has major implications in breast cancer risk and breast cancer chemoprevention. This study aimed to investigate the feasibility of accurate, low-cost quantification of MD *in vivo* without ionising radiation.

We used single-sided portable nuclear magnetic resonance ("Portable NMR") due to its low cost and the absence of radiation-related safety concerns. Fifteen (*N*=15) healthy female volunteers were selected for the study and underwent an imaging routine consisting of 2D X-ray mammography, quantitative breast 3T MRI (Dixon and T_1-based 3D compositional breast imaging), and 1D compositional depth profiling of the right breast using Portable NMR. For each participant, all the measurements were made within 3-4 hours of each other. MRI-determined tissue water content was used as the MD-equivalent quantity. Portable NMR depth profiles of tissue water were compared with the equivalent depth profiles reconstructed from Dixon and T_1-based MR images, which were used as the MD-equivalent reference standard.

The agreement between the depth profiles acquired using Portable NMR and the reconstructed reference-standard profiles was variable but overall encouraging. The agreement was somewhat inferior to that seen in breast tissue explant measurements conducted *in vitro*, where quantitative micro-CT was used as the reference standard. The lower agreement *in vivo* can be attributed to an uncertainty in the positioning of the Portable NMR sensor on the breast surface and breast compression in Portable NMR measurements.

The degree of agreement between Portable NMR and quantitative MRI is encouraging. While the results call for further development of quantitative Portable NMR, they demonstrate the in-principle feasibility of Portable NMR-based quantitative compositional imaging *in vivo* and show promise for the development of safe and low-cost protocols for quantification of MD suitable for clinical applications.

1.   INTRODUCTION

1.1. *Mammographic density*

Mammographic density (MD), which is also known as breast density, is an indicator of breast tissue composition - namely, the relative content of fibroglandular tissue (FGT), which comprises stroma and epithelial tissue. The name "MD" originates from X-ray mammography, the medical imaging technique traditionally used to assess breast density. Because water is a more efficient absorber of X-rays than fat, FGT is relatively radiodense and adipose tissue is relatively radiolucent. Consequently, regions of the breast with a high proportion of FGT appear bright (high intensity) on the mammogram, corresponding to areas of high MD (HMD regions). Conversely, regions with a high content of adipose tissue appear dark (low intensity) and correspond to areas of low MD (LMD regions) [1-4].

Mammography is a 2D projectional imaging technique, and therefore the mammographically measured percentage of "dense" tissue (MD score) typically applies to the breast as a whole. Alternatively, three-dimensional approaches to MD quantification (e.g. MRI, see section 1.2) enable the measurement of volumetric fraction of FGT, which can be considered a MD-equivalent quantity [5-7]. Importantly, such approaches enable the measurement of the spatial map of MD (or its equivalent), rather than just the breast-averaged MD score yielded by conventional mammography.

The other limitation of the traditional X-ray mammography is its reliance on ionising radiation, which limits when and how frequently mammography is clinically justifiable. Therefore, while mammography remains the clinical "gold standard" for MD assessment, there is a significant interest in developing non-ionising alternative techniques that may measure MD-equivalent quantities.

1.2. *Non-ionising imaging of breast density*

Ultrasound [8,9], bioimpedance [10], and transillumination [11,12] have all been proposed as alternative imaging techniques for measuring MD-equivalent quantities [13,14]. However, it is Magnetic Resonance Imaging (MRI) that stands out as an attractive modality for MD quantification [15-17]. MRI is particularly promising in this respect because it offers great signal editing flexibility and several contrast mechanisms suitable for distinguishing FGT and adipose tissue. Chemical shift imaging (CSI), and most notably the Dixon CSI scheme,

enables quantification of fat and water based on the difference between the NMR chemical shifts of water and methylene lipid protons (~3.5 ppm), which can be accomplished even in the absence of reliable spectral separation of the two components [18,19]. In the original two-point Dixon scheme [18], two images with slightly different echo times are acquired: one where the magnetisation of water and lipid methylene protons is in-phase, and the other, where the two magnetisation vectors are at 180º to each other ("out-of-phase"). These two "raw" images are then used to reconstruct the 3D maps of fat and water signal intensities, thus providing a spatially resolved compositional map of the tissue that serves as a proxy for the distribution of mammographic density. Another common approach to quantitative compositional imaging is based on differences between the spin-relaxation times (usually T_1) of fat and water. This can involve either the measurement of a map of the apparent T_1 and translating it into tissue composition using a calibration curve; or alternatively, several inversion recovery-edited images with different inversion times can be acquired, from which fat and water compositional maps are reconstructed. Good quantitative agreement has been demonstrated between breast density values measured *in vivo* using MRI pulse sequences exploiting different contrast types [5]. Good accuracy of Dixon and T_1-based MRI FGT quantification has also been demonstrated in anthropomorphic breast phantoms [6]. Finally, a number of studies have demonstrated good agreement between quantitative MRI and conventional mammographic measurements of breast density [17,20-25].

1.3. Portable NMR

At the same time, the relatively high cost of MRI remains an impediment to its use for routine clinical monitoring applications. Single-sided portable Nuclear Magnetic Resonance ("Portable NMR") [26-28] is a low-cost technique that is based on the same fundamental physics as MRI and offers many of the quantitative measurement capabilities of MRI. In particular, Portable NMR offers the ability to quantify spin-relaxation and diffusion, i.e. the exact physical properties that underpin reliable quantification of MD in conventional breast MRI. Portable NMR has the advantages of low purchasing and running costs and low maintenance, largely due to the absence of superconducting magnets, which obviates the need for cryogens. Importantly, the utility of Portable NMR for biomedical imaging has been demonstrated in a wide range of applications [28-46].

Our previous work has demonstrated the suitability of Portable NMR for quantification of MD-equivalent density in breast tissue explants *in vitro* [47-50]. In those measurements,

several approaches have been explored: (i) Saturation-recovery measurement of the apparent T_1 value (suitable when longitudinal spin-relaxation is monoexponential); (ii) apparent T_2 relaxation spectrum: Measurement of the Carr-Purcell-Meiboom-Gill (CPMG) echo train followed by an inverse Laplace transform (ILT) (requires a "long" CPMG echo time in order to separate the Fat and Water peaks in the relaxation spectrum); (iii) CPMG measurement of the tissue-average T_2 value (requires a "short" CPMG echo time and a monoexponential decay of transverse magnetisation); (iv) Stimulated-echo measurement of the diffusion attenuation curve followed by biexponential least-squares fitting analysis. Each approach was demonstrated to agree with the two-component tissue composition model, whereby the relative NMR signal contributions of tissue water and lipids ("fat") represented the relative amounts of FGT and adipose tissue, and consequently MD [47-49]. Approaches (ii) and (iv) enable a direct quantification of MD in terms of tissue water content ("Water Fraction", WF). Approaches (i) and (iii) require a calibration curve to translate the NMR spin-relaxation time constants into tissue composition. We found that approaches (ii) and (iv) tended to produce the best agreement with the reference standard (micro-CT), and approach (ii) offered the best perceived combination of speed and accuracy. Consequently, approach (ii) (which for brevity we will refer to as the CPMG/ILT approach) was employed in a subsequent study of hormonal effects on mammographic density in breast tissue explants [51].

In the present study, we extend the CPMG/ILT approach to quantification of MD *in vivo*. Portable NMR was used to measure the depth profiles of MD-equivalent breast density in 15 healthy female volunteers. These depth profiles were compared with the MD-equivalent reference standard - depth profiles of tissue water reconstructed from three-dimensional Dixon and quantitative inversion-recovery MR images. We discuss here the degree of quantitative agreement between Portable NMR and the reference standard, as well as the prospects for potential Portable NMR-based quantitative breast tissue imaging. We see this study as an important step towards introducing Portable NMR into the realm of clinical applications. Although pioneering Portable NMR studies *in vivo* were carried out by Bluemich and co-workers well over a decade ago [52,53], to our knowledge, the present study is only the second structured human clinical trial involving Portable NMR [54] and the first application of Portable NMR to breast imaging *in vivo*.

2. MATERIALS AND METHODS

2.1. Volunteer participant cohort

The study was approved by Metro South Health Human Research Ethics Committee (HREC/2018/QMS/45443), and also administratively by QUT Human Research Ethics Committee (1800001123). Volunteer participants for the study were recruited through an advertisement placed on the Princess Alexandra Hospital Research Foundation Facebook page. Premenopausal healthy females aged between 18 and 50 were considered eligible in the absence of exclusion factors. Participants were excluded if: (i) they were pregnant or suspected they could be pregnant; or (ii) they have ever been diagnosed with breast malignancy; or (iii) they had any devices or materials in their body that were not compatible with MRI. Successfully recruited participants were not paid but were reimbursed for the costs of hospital parking. A total of $N = 15$ participants were successfully recruited for the study. All participants underwent the scanning protocol described in Section 2.2.

2.2. Study design

The volunteer participants underwent a scanning protocol that consisted of: (i) conventional 2D X-ray mammography of the right breast; (ii) 1D compositional depth profiling of the right breast using Portable NMR, as described in Section 2.3; and (iii) quantitative breast MRI that included T_1-based and two-point Dixon 3D compositional breast imaging (Section 2.4). In order to avoid a potential comparison bias due to menstrual cycle-related MD dynamics, all the measurements for each participant were made on the same day within 3-4 hours of each other.

Breast Imaging Reporting and Data System (BI-RADS) breast density category was determined for each participant from the 2D mammograms. For participants 4 – 9 this was done automatically by Volpara breast density software algorithm version 1.5.4.0 (Volpara Health, Wellington, New Zealand); for the remaining participants the scoring was performed by a clinical radiologist (TL). The 2D mammograms were used for qualitative reference only and were not part of the quantitative analysis. The 3T MR images (T_1 and Dixon) were post-processed to reconstruct 3D compositional maps of the breast, followed by the reconstruction of 1D profiles of fat and water content equivalent to those acquired using Portable NMR (see Section 2.7). This enabled a direct comparison between 3T MRI and Portable NMR data. The three sets of 1D compositional depth profiles (Portable NMR, Dixon and T_1) were compared

to each other using the similarity analysis described in Section 2.8 and Bland-Altman analysis [55].

2.3. Single-sided Portable NMR measurements

Portable NMR measurements were performed using a PM25 NMR-MOUSE instrument connected to a Kea^2 spectrometer (Magritek, Aachen, Germany). The instrument is illustrated in Figure 1(a). NMR-MOUSE is a single-sided NMR scanner [56] based on permanent magnets that provide a horizontal magnetic field B_0 = 0.31 T (^{1}H Larmor frequency 13.18 MHz) and a vertical permanent field gradient g = 7.5 T/m. A single surface coil provides excitation and signal detection. The sensing slice is a horizontal disc-shaped volume approximately 35 x 35 x 0.06 mm^3 (the short dimension being the direction of the vertical gradient). 1D depth profiling is achieved by varying the vertical position of the sensing slice using a lift with an electronically controlled high-precision stepper motor, as described previously [47]. This moves the entire magnet and sensor coil assembly in the z direction in Fig. 1(a), while the sample remains stationary on the sample stage; the sensing slice is thus moved up or down within the sample. In the configuration used in the present study, the sensing slice was fixed at 20.8 mm above the sensor coil, corresponding to the maximum tissue penetration depth of 20.8 mm.

The setup of the Portable NMR breast measurements *in vivo* is illustrated in Figure 1(b). The scan bed was a wooden massage table modified with a rectangular aperture in the upper-torso area. The NMR-MOUSE instrument was positioned in the aperture such that its sample stage was aligned with the top surface of the massage table. The participants, wearing a T-shirt provided by TRI and own brassiere, were positioned prone over the aperture such that the right breast was flattened against the NMR-MOUSE sample stage. The T-shirts [illustrated in Fig. 2(a)] were all of the same type and had a horizontal stripe pattern in order to assist accurate topographical localisation of the measurement site. A localisation marker (a small coloured sticker ~2 cm diameter), placed on the participants' clothing in the right upper-outer quadrant of the right breast, was aligned with the centre of the sensor coil. All Portable NMR measurements were made at this topographical location, at tissue penetration depths ranging from 20.8 mm to -1.2 mm inclusive (referenced to the NMR-MOUSE sample stage) in increments of -2 mm. The depth profiling was achieved moving the sensor assembly in the vertical dimension, as described above: the topmost position of the sensor assembly (pressed against the participant's skin surface) corresponded to the maximum measurement depth

(20.8 mm), while lowering the sensor assembly moved the sensing slice in the outward direction relative to the breast. The depth profiling procedure took approximately 20-25 minutes. The outermost sensing slice (-1.2 mm depth) typically produced noise only. The Portable NMR depth profiles therefore typically included 11 depth points with a non-zero signal. No corrections were taken for the thickness of the clothing worn by the volunteer participant.

At each depth point, the amount of fat and water in the sensing slice was quantified using the CPMG/ILT approach. Carr-Purcell-Meiboom-Gill (CPMG) decay curves were acquired with the parameters TE = 700 µs, NE = 1000 echoes, DW = 0.5 µs and NP = 32 complex points per echo, NS = 4 averages. The TE value used (700 µs) had previously been established to be in the "long-TE" limit sufficient for reliably separating Fat and Water peaks in the ILT apparent transverse relaxation spectra. Both "90°" and "180°" RF pulses were rectangular of 27 µs duration. The corresponding sensing slice thickness (defined as the full width at half-height of the central lobe of the Sinc-like excitation profile obtained from the Bloch equations) was 63 µm for the 90° excitation pulse and 70 µm for the 180° refocusing pulse. The recovery time, TR = 20 s, was chosen to create a failsafe safety margin with respect to power deposition in breast tissue. The actual Specific Absorption Rate (SAR) was not measured in the Portable NMR measurements.

For each CPMG measurement, the apparent T_2 relaxation spectrum was computed using a regularised one-dimensional inverse Laplace transform (ILT), as described in detail in the literature [48,57]. The relative fractions of tissue water and fat were then determined by integrating the two peaks and calculating their relative areas.

2.4. Quantitative 3T MRI measurements

Quantitative breast MRI was performed at Princess Alexandra Hospital on a Siemens Prisma 3T scanner with a standard bilateral breast coil. For each participant, the following MRI datasets were acquired:

(i) A two-point Dixon imaging dataset [18,19] acquired using 2D Turbo SE protocol. The typical imaging parameters were: Turbo factor = 15, TE = 81 ms, recovery time TR between 4.6 and 5.8 s (varied between volunteer participants), NS = 1 average, axial slice orientation, number of slices between 27 and 34 (varied between participants), slice thickness 4 mm, slice

separation 5 mm (1 mm gap between slices), FOV $(350 \text{ mm})^2$, matrix NR x NP = 384 x 384, in-plane resolution $(0.91 \text{ mm})^2$, pixel bandwidth 930 Hz. From each pair of Dixon images, fat-only and water-only images were reconstructed using the built-in Siemens protocol; the latter images were used as the primary tissue composition reference;

(ii) Three T_1-weighted inversion recovery-prepared, 2D TurboSE-acquired datasets with the recovery times TI = 210 ms, 690 ms and 3000 ms, corresponding to fat-suppressed, water-suppressed and full-intensity images, respectively. The "fat-suppressed" image for Participant 1 was acquired with TI = 290 ms. The typical imaging parameters were: Turbo factor = 17, TE = 75 ms, recovery time TR between 3.6 and 11.8 s (varied between participants and TI runs), NS = 2 averages, axial slice orientation, number of slices between 27 and 34 (varied between participants), slice thickness 4 mm, slice separation 4.8 mm (0.8 mm gap between slices), FOV $(340 \text{ mm})^2$, matrix NR x NP = 448 x 448, in-plane resolution $(0.76 \text{ mm})^2$, pixel bandwidth 320 Hz. From each triplet of the T_1-weighted images, 3D fat and water contents maps were reconstructed as described in Section 2.5; these maps were used as a secondary tissue composition reference.

2.5. Quantitative analysis of T_1-weighted MR images

Assuming a perfect 180° inversion pulse and a steady state with respect to TR, the signal intensity of the i-th chemical component in an inversion recovery-edited image is

$$A_i\left(\text{TI}\right) = \frac{S_i\left(\text{TI}\right)}{S_i\left(0\right)} = 1 - \frac{2}{1 + \exp\left(-\text{TR}/T_{1i}\right)} \cdot \exp\left(\frac{-\text{TI}}{T_{1i}}\right) \tag{1}$$

where T_{1i} is the longitudinal spin-relaxation time constant of the i-th component, TI is the inversion time, TR the repetition time, and $S_i(0)$ is the full signal intensity of the respective component. The derivation of Eq. (1) is shown in Supplementary Material. The empirically known signal nulling times (TI_{nullF} = 210 ms, TI_{nullW} = 690 ms) yield the estimates of the respective T_1's: T_{1F} = (210 ms)/ln(2) = 303 ms, T_{1W} = (690 ms)/ln(2) = 995 ms. Therefore, the coefficients A_i can be regarded as known quantities in that they can be calculated for any given combination of TI and TR.

Assuming that fat and water are the only two contributors to MR signal in breast tissue, the total signal in a magnitude image is given by:

$$S_T\left(\text{TI}\right) = \left| A_F\left(\text{TI}\right) \cdot S_{0F} + A_W\left(\text{TI}\right) \cdot S_{0W} \right| \tag{2}$$

Given the images measured at three TI values (TI = 210, 690 and 3000 ms), Eq. (2) presented

an over-determined system with three data points [$S_T(210)$, $S_T(690)$ and $S_T(3000)$] and two unknowns (S_{0F} and S_{0F}). Correspondingly, the values of S_{0F} and S_{0F} were determined for each voxel by least-squares fitting. These were then normalised to represent the fractions of fat and water in a given voxel, and by inference, the relative amounts of FGT (water) and adipose tissue (fat).

For a given ROI, the relative water fraction (WF) was then determined as

$$\mathrm{WF} = \frac{S_W}{S_W + S_F} \qquad (3)$$

where S_F and S_W are the total amounts of fat and water, respectively, within the ROI. The value of WF was taken as the MD-equivalent quantity for the given ROI.

2.6. Quantitative analysis of Dixon MR images

The Dixon imaging protocol implemented on the Siemens Prisma scanner included a built-in reconstruction of the Fat and Water signal maps. Therefore, the only post-processing required for the Dixon images was the reconstruction of the water fraction (WF) depth profiles as described in Section 2.7.

2.7. Reconstruction of 1D depth profiles from 3D MR maps

In order to directly compare 1D Portable-NMR depth profiles with the three-dimensional 3T MRI reference standard, the 3T MRI data was used to reconstruct 1D depth profiles equivalent to the respective Portable-NMR measurement. This was done as follows:

(i) The location of the centre of the Portable NMR sensor coil was identified in a high-intensity MR image based on the photograph of the participant with the sensor location marker [the "yellow dot" in Fig. 2(a)]. The distance from the nipple to the location marker was measured by counting the stripes on the T-shirt, and the direction of the line connecting the two points was noted; the same distance in the same direction was then measured in the MR image to identify the location corresponding to the position of the sensor coil in Portable NMR measurements;

(ii) A (curved) 3D skin surface was rendered in the MR image around the location of the sensor coil identified in (i);

(iii) The normal to the rendered skin surface at the location of the sensor was calculated;

(iv) A circular area of 3.5 cm diameter was identified on the skin surface;

(v) The area identified in step (iv) was translated along the normal identified in step (iii) by +50 μm and −50 μm, thus creating a thin curved slab parallel to the skin surface;

(vi) The slab identified in step (v) was then translated along the normal identified in step (iii) in 2 mm increments until the maximum depth of 20.8 mm, which corresponded to the maximum penetration depth of the Portable NMR sensor.

This process is illustrated in Fig. 2(b). For each slab position, the MRI voxels intersecting the slab were identified. The total amounts of fat and water within each slab were then calculated as the sum of the respective signals over the voxels intersecting the slab. The relative water fraction WF within each slab was then calculated according to Eq. (3).

2.8. Comparison of Portable NMR depth profiles with 3T MRI reference standard

In order to quantify the degree of agreement between the depth profiles measured using Portable NMR and those reconstructed from 3T MRI data, a "whole-of-profile" similarity index SI was used:

$$\text{SI} = 1 - \frac{\sum_{i=1}^{n_d} |f_i - g_i| \cdot \Delta d}{(\Delta d \cdot n_d)} \tag{4}$$

where $\Delta d = 2$ mm is the step of the depth profile, n_d is the number depth steps and $\Delta d \cdot n_d$ is the maximum depth. The physical range of the compared quantities f and g in Eq. (4) is assumed to be between 0 and 1, corresponding to the physically meaningful range of water fraction values. In the case when the profiles f and g are identical, the value of SI is 1. Conversely, when the two profiles are the physical opposites of each other (e.g., profile f has the constant value of 1 and profile g has the value of 0), the value of SI is 0. In general, the value of (1 − SI) has the physical meaning of the mean absolute difference between the two curves, normalised to the size of the physical range of the quantity measured (in the case of the water fraction ranging between 0 and 1, the normalisation factor is 1). The index SI also has a simple and intuitive graphical interpretation illustrated in Fig. 3.

3. RESULTS

3.1. Portable NMR measurements

A representative Portable NMR single-depth dataset (Participant 11, depth 16.8 mm), comprising the CPMG decay curve and the corresponding T_2 relaxation spectrum, is shown in Fig. 4. All acquired CPMG decay curves exhibited a baseline well within the noise level and were sampled to the baseline. The typical SNR was ~5. The individual CPMG echoes were integrated by adding the intensities of the 32 points in the given echo; a single integrated echo corresponds to a single point in Fig. 4(a). The T_2 relaxation spectra [Fig. 4(b)] typically exhibited two peaks: the water peak centred at $T_2 \sim$ 5-10 ms and the fat peak centred at $T_2 \sim$ 90-100 ms. In some measurements only the fat peak was present, indicating extreme-LMD locations. Extreme-HMD scenario (only the water peak present) was observed only in a single measurement.

3.2. Dixon MRI measurements

A representative Dixon MRI dataset (a single axial slice from Participant 11) is illustrated in Fig. 5. The primary data acquired were the in-phase and out-of-phase images [Figs. 5(a) and 5(b), respectively], which typically exhibited comparable prevailing intensities. From these, the water and fat maps [Figs. 5(c) and 5(d), respectively] were automatically reconstructed by the Siemens software. Table 1 shows the water fraction averaged over the right breast for each study participant, together with the BI-RADS category, as a reference.

3.3. Quantitative T_1-weighted MRI measurements

A representative T_1-weighted MRI dataset (a single axial slice from Participant 11) is illustrated in Fig. 6. The intensity of the fat-nulled image [Fig. 6(a)] was dominated by the water signal; the intensity of the water-nulled image [Fig. 6(b)] was dominated by the fat signal; and the "full-intensity" image [Fig. 6(c)] represented the fat and water signals at 90-95% of the full intensity, depending on the TR value. The intensity differences between the three primary images enabled the determination of the relative fat and water signal amplitudes for each voxel and therefore the reconstruction of the compositional maps similar to Figs. 5(c) and (d), as described in Section 2.5.

3.4. Depth profiles reconstructed from MRI data

The reference-standard profiles were reconstructed from 3T MRI data so as to match the

topographical location and the depth points of the respective Portable-NMR depth profile. This enabled a direct and straightforward comparison of the Portable NMR results with the reference standard. Two representative sets of depth profiles, one showing a relatively good agreement and another showing a relatively poor agreement between Portable NMR and MRI, are shown in Fig. 7. Quantitative comparison of the depth profiles with the reference standard was based on the similarity index SI defined in Eq. (4). The SI values for each participant and each comparison pair are shown in Table 1. The profile-average water fraction values measured from the Dixon data are also shown in Table 1 as a reference.

The results of pairwise Bland-Altman analysis are presented in Table 2. The full set of depth profiles is shown in Supplementary Material Fig. SF2, and the full set of pairwise Bland-Altman plots is shown in Supplementary Material Fig. SF3.

4. DISCUSSION

4.1. Motivation and previous work

Mammographic Density is clinically important for two main reasons: (i) High MD represents an independent and significant risk factor for breast cancer (BC) [58-62]; and (ii) High MD also acts as a masking factor in mammographic screening, often making mammographic detection of breast cancer lesions difficult, and resulting in higher numbers of interval cancers detected after a negative mammogram [61,63,64]. The chance of developing breast cancer is 4-6 times higher for women in the highest MD quartile than for those in the low-MD group [15,65], and approximately double that of the general population [58,62]. As a result, provision of MD information to women is now legislated in 38 States and the District of Columbia in the United States of America, as well as British Columbia in Canada [66]. Many other countries are considering similar reporting guidelines [67], and BreastScreen in Western Australia has provided MD information for over a decade [68].

Besides the assessment of breast cancer risk, accurate quantification of MD is of potential clinical interest in the contexts of understanding the biophysical and molecular mechanisms underpinning breast cancer proliferation as well as patient-specific prediction of the efficacy of hormonal anticancer and cancer-prevention treatments. Dynamic changes in MD over 12-18 months have been found to be a predictive biomarker of the efficacy (and the eventual success or failure) of antiestrogen chemoprevention and breast cancer treatment [69-71]. Therefore, there is potential clinical value in being able to perform high-frequency quantitative monitoring of MD.

However, traditional X-ray mammography is ill-suited to this task, most significantly because it involves ionising radiation, which limits how frequently it can be used in a given patient [72]. This limitation provides the clinical need for the development of non-ionising alternative techniques for breast screening based on the measurement of MD-equivalent quantities. Magnetic Resonance provides an attractive and flexible platform for the development of such techniques.

In our previous work we have established the Portable NMR-based methodology for quantification of MD-equivalent breast density in breast tissue explants *in vitro* [47-49]. In that approach, which we termed Compositional Imaging, the relative amounts of fat and

water measured using Portable NMR are taken to represent the relative amounts of adipose tissue and FGT, respectively, in the breast tissue. We have previously demonstrated a good reliability of this approach *in vitro*, with the relative water fraction measured using Portable NMR agreeing with the reference standard (micro-CT) to within 5-10 percentage points [49]. In the present study we extend this methodology to applications *in vivo*. The participants of the present study were healthy volunteers with no medical indication for a CT scan. Therefore, the reference standard used in the present study was MRI – a non-ionising imaging modality capable of reliably quantifying tissue water content, which is commonly used as a MD-equivalent quantity [5-7].

4.2. Portable NMR measurements: technical aspects

The Portable NMR instrument used in the present study, NMR-MOUSE PM25, was able to be configured for several maximum-penetration depths ranging from 5.9 mm to 26 mm. However, inherent in the design of the sensor was an inverse relationship between penetration depth and the absolute amplitude of the detected signal, and consequently the Signal-to-Noise Ratio (SNR). The configuration with the penetration depth of 20.8 mm was chosen as the perceived optimal compromise between these two factors: this penetration depth of 20.8 mm was sufficient to scan most of the breast thickness in the upper-outer quadrant of the breast, where the measurements were taken; and on the other hand, the coil sensitivity was sufficient for achieving as acceptable SNR in NS = 4 scans.

As seen from Fig. 4(a), the typical SNR of the Portable NMR CPMG decays was ~10. This SNR is consistent with Portable NMR CPMG relaxometry studies found in the literature and sufficient for a reliable ILT inversion of the CPMG decay. While at the face value this SNR appears relatively low compared to MR imaging, two factors ensure the robustness of the relaxation spectra illustrated in Fig. 4(b): regularisation of the data built into the ILT procedure and the use of a large number of CPMG echoes (NE = 1000). The robustness of the ILT-inverted relaxation spectra under the measurement conditions used was verified by us previously using phantoms and noisy synthetic data. It was also checked that the apparent Fat:Water ratio was not sensitive to the ILT regularisation parameter.

4.3. Accuracy of Portable NMR positioning and target-volume identification in vivo

While quantitative compositional Portable NMR has been successfully applied and validated *in vitro* [51], several additional factors must be taken into account in its applications *in vivo*.

The first factor is the spatial localisation of Portable NMR measurements. The Water Fraction (WF) depth profiles measured using Portable NMR represent a specific topographical location on the breast, as opposed to the entire breast imaged in mammography or conventional MRI. This is a direct result of the physical design of the single-sided Portable NMR sensor coil, which can be approximated as a surface coil and consequently provides signal detection over an area roughly equal to the size of the coil itself. Therefore, the MD metrics derived from Portable NMR are inherently local metrics; as such, they should not be directly compared to BI-RADS scores or breast-averaged FGT content derived from conventional mammography and MRI, respectively. It is well-known (and also illustrated by Figs. 5 and 6) that breast tissue composition is spatially heterogeneous; therefore, a breast-averaged MD value is not necessarily representative of a WF measurement taken at a specific location (and *vice versa*). Indeed, Table 1 reveals significant differences between breast-averaged and local profile-averaged WF values derived from the same technique (Dixon MRI): the profile-averaged WF values are consistently higher than the breast-averaged values due to the fact that the location chosen for Portable NMR measurements (upper-right quadrant) has a known tendency to exhibit relatively high local MD. For this reason, the quantitative comparison between Portable NMR and MRI in the present study was between *local* MD-equivalent values measured using different techniques: i.e., individual depth points from Portable NMR depth profiles were compared with the corresponding points in the depth profiles reconstructed from MRI data.

While local MD-equivalent measurements are not a substitute for conventional whole-breast measurements of MD, they can potentially have an important role in clinical breast imaging. To use an example from section 4.1, when MD is used as a predictor of antiestrogen chemoprevention treatments, it is the temporal dynamics of MD that is of interest, not the absolute value of MD. In this context, local MD-equivalent measurements taken consistently at the same topographical location could be used as a proxy for the dynamics of whole-breast MD.

The second factor to be taken into account when comparing breast tissue composition derived from Portable NMR *vs* MRI is that single-sided portable NMR is a depth profiling, rather than a 3D imaging, technique: It affords spatial resolution in the "depth" dimension but provides no lateral-dimension spatial resolution within the sensing slice. Conversely, the reference MR images used in the present study were 3D images that covered the entire

volume of the breast with the spatial resolution ~5 mm in the slice-selection dimension and ~1 mm in the Read and Phase dimensions. A quantitative comparison between Portable NMR and MRI required identifying the MRI voxels that contributed to the signal from a given reconstructed Portable-NMR slice, then adding the signal intensities of the respective voxels to emulate a signal from the reconstructed slice, thus ensuring that the comparison is carried out between equivalent local volumes of breast tissue. An added complication entailed by this approach is partial voluming: because none of the MRI voxels intersecting with the target slice are fully contained in the latter, the reconstructed slice inevitably represents a significantly larger physical volume than the actual Portable NMR sensing slice; this further complicates the comparison between Portable NMR and reference MRI techniques.

The accuracy of topographical positioning of the Portable NMR sensor, as well as the accuracy of identifying its position in 3D MR images, is another factor to consider when comparing the results from the two techniques. In the absence of quantitative geodesic approaches capable of unambiguously mapping the physical surface of the breast to the MR image, and *vice versa*, the position of the Portable-NMR sensor in the MRI frame of reference is subject to an uncertainty of the order of several cm. In the case of a topographically heterogeneous distribution of MD within the breast, this can potentially lead to distortions in the MRI-reconstructed depth profiles.

The other factor likely to limit the quantitative agreement between Portable NMR and MRI is the difference in the compressive state of the breast between the two techniques. The reference-standard MR breast images were acquired on pendant non-compressed breasts. On the other hand, Portable NMR depth profiles were acquired on compressed breasts, with the participant's right breast being pressed against the sensor [see Fig. 1(b)]. Such compression has two potential geometrical effects: (i) The breast skin surface in the scanned region is transformed from curved to planar; and (ii) compression may also distort the distances measured from the skin surface into the breast tissue.

All these factors complicate the comparison between the depth profiles directly acquired in Portable NMR and the equivalent profiles reconstructed from MRI data. Some of these factors are unique to breast measurements *in vivo* and were not present in breast tissue explant measurements *in vitro*. Furthermore, the present Portable NMR measurements *in vivo* involved a significantly larger sensitive volume than the breast tissue explants used for

measurements *in vitro* [49]. While this factor is not necessarily unique to measurements *in vivo*, it does have potential implications for quantitative accuracy because some of the Portable NMR signal *in vivo* arises from tissue regions far from the isocentre of the sensor. Considering the combination of these factors, quantitative agreement between Portable NMR and the reference standard in the present study can be expected to be inferior to that observed *in vitro*.

4.4. *Agreement between Portable NMR and MRI-reconstructed depth profiles*

The degree of agreement between WF depth profiles obtained from Portable NMR and from reference MRI datasets was evaluated using the similarity index SI given by Eq. (4) and also using pairwise Bland-Altman analysis. Bland-Altman analysis has previously been successfully used in biomedical imaging literature for comparison of depth profiles derived from two different techniques [73]. The similarity index SI can, in fact, be viewed as a logical extension of Bland-Altman analysis because, similar to the latter, SI is based on the differences between the individual data points in the two profiles. The distinction between SI and Bland-Altman analysis is that in the former the mean difference is expressed in relative terms, as opposed to Bland-Altman's absolute standard deviation.

Tables 1 and 2 reveal that the typical limit of quantitative agreement between Portable NMR and 3T MRI is ~20 percentage points. This is indeed inferior to the breast tissue explant measurements *in vitro*, where a typical agreement with the reference standard was 5-10 percentage points.

Nevertheless, we have found several observations encouraging. The first is a good agreement between the average value of MD measured from Portable-NMR and MRI-reconstructed depth profiles. The second, even more encouraging, observation is the broad agreement between qualitative profile features, such as the direction of change of MD from superficial to deep tissue, or (in some participants) the presence of "dips" in the profiles. The profiles of Participant 14, which are shown in Fig. 7(b), fail to exhibit such an agreement; however, this case is extreme, and in most participants there was a clear qualitative concordance between Portable NMR and MRI depth profiles.

We also find it encouraging that the Bland-Altman profiles shown in Fig. SF3 (Supplementary Material) do not tend to exhibit a prevailing "tilt" towards either high-WF or

18

low-WF end of the range. Importantly, the distribution of the errors in the Bland-Altman plots appears random and, with a few exceptions, the bias tends to be lower than the Bland-Altman standard deviation. This suggests that the limited agreement between different Portable NMR and reference MRI measurements is due to complex and heterogeneous morphology of breast tissue rather than some inherent limitations of Portable NMR.

Finally, while the quantitative agreement between Portable NMR and reference MRI is limited, we note that it is comparable to the agreement between the two reference MRI techniques themselves, T_1-weighted and Dixon. While the agreement between the two MRI techniques tended to be better than that between Portable NMR and MRI, the WF depth profiles reconstructed from T_1-weighted and Dixon data tended to exhibit discrepancies ~15 percentage points. This further suggests that the limited agreement between different techniques is due in large part to the morphological complexity of breast tissue. It also calls for the development of more sophisticated reference MRI techniques for future studies. While both T_1-weighted and Dixon MR imaging have been used and successfully validated for MD quantification [5,6], they were used in the context of whole-of-breast (or whole-of-phantom) assessment of MD, not for location-specific MD assessment. Because location-specific assessment is performed over a relatively small volume, it is more sensitive than whole-of-breast MD measurement to noise and to partial-voluming that depth profile reconstruction inevitably entails. While a detailed discussion of alternative reference techniques is outside the scope of the present study, possible approaches include using identical spatial resolution in both T_1 and Dixon measurements; reconstruction of depth profiles with MRI voxels weighted by their overlap volume with the target slice; and the use of larger numbers of raw datasets in both T_1 and Dixon measurements (i.e., a multi-point rather than 2-point Dixon and the acquisition of the full inversion-recovery curve instead of just three TI values for T_1-weighted datasets). The latter approach could potentially push the imaging times beyond what is compatible with a human clinical trial; this suggests that the use of anthropomorphic breast phantoms would be beneficial for further technique development.

4.5. *Power deposition in Portable NMR measurements*

The Specific Absorption Rate (SAR) was not directly measured in the Portable NMR measurements presented. Nevertheless, the value of SAR can be estimated based on the model of RF power deposition in the low-frequency MRI limit used by Bottomley and

Edelstein [74]. The details of SAR estimation are presented in Supplementary Material, and the resulting value of SAR in the layer of tissue adjacent to the RF sensor coil was 2.4 W/kg.

The key parameters required for the calculation of SAR using Eq. (SM8) are the value of B_{RF}, the size of the RF coil (R) and the resistivity of the tissue (ρ). As shown in Supplementary Material, the RF coil of the NMR-MOUSE instrument can be approximated as an ideal loop-with-current coil for the purposes of SAR calculation. Therefore, other parameters being equal, the greatest power deposition can be expected to occur in the layer of tissue immediately adjacent to the Portable NMR sensor (skin), where B_{RF} is the greatest. The value of tissue resistivity used for the SAR calculation ($\rho = 2.0$ $\Omega \cdot$m, see Table ST2) was selected to represent a low-end estimate for both skin and breast tissue at 15 MHz [75]; the actual tissue resistivity is most likely to be higher than this assumed value. We also note that the low-frequency SAR limit used in ref. [74] tends to overestimate the value of SAR both compared to direct measurements and to the SAR value calculated using more sophisticated models that take into account variation of the RF field amplitude within the tissue [76]. Therefore, the SAR value of 2.4 W/kg is likely an over-estimate.

Even this high estimate of SAR is well within the International Commission's on Non-Ionizing Radiation Protection (ICNIRP) safety guideline for local SAR values, 10 W/kg in any 10 grams of tissue [77]. This suggests that the SAR value in our Portable NMR CPMG measurements contains a generous safety margin, and there is a significant room for increasing the SAR, for example by shortening the TR while keeping the echo train parameters constant.

4.6. Prospects of Portable NMR for MD quantification in vivo

The broad agreement observed between Portable NMR and MRI depth profiles is encouraging. It is, however, helpful to evaluate the precision and accuracy of Portable NMR in the context of its prospective clinical applications. One such application is the monitoring of dynamic MD changes in hormonal anticancer or cancer-prevention therapy [47], where a transient reduction in MD (typically ~10% over 1-1.5 years) can herald the eventual success of the therapy. This would require MD to be able to be quantified *in vivo* with the precision and reproducibility of ~5 percentage points or better in order to reliably identify the changes in question, or lack thereof. The focus of the present study was not precision but accuracy,

i.e. the ability of Portable NMR to match the reference standard (MRI). In itself, a high accuracy is not necessarily a prerequisite for dynamic monitoring of MD because the presence of a constant absolute bias in the measured values would not affect the dynamic changes being observed. Nevertheless, the present results can also be used to gauge the precision of the Portable NMR protocol used in our study. For example, in Fig. 7(b) it can be seen that the Dixon-measured MD profile (red dots) exhibits a smooth behaviour, indicating a gradual change in MD from superficial to deep breast tissue. At the same time the Portable NMR-measured MD profile (blue dots) does not vary smoothly but exhibits high spatial-frequency oscillations. We hypothesise that these oscillations are indicative of the precision of the measurement rather than the underlying MD pattern; however, a detailed analysis of precision and reproducibility of Portable NMR measurements *in vivo* will be the subject of a follow-up study.

We note that the scan times required under the present Portable NMR protocol (20-25 minutes per depth profile) are at the upper limit of what could be considered clinically acceptable. However, given the apparent generous safety margin built into our Portable NMR SAR value, it is likely that the Portable NMR protocol can be shortened to less than 10 min by reducing the TR 3-to-4-fold without compromising power deposition safety.

Overall, the observed 20 percentage points typical discrepancy between Portable NMR and reference MRI calls for avenues for improving the quantitative performance of the methodology before it can be viewed as viable for reliable MD quantification *in vivo*. The following avenues of future research are apparent:

(i) A systematic study of the precision and reproducibility of MD quantification using Portable NMR would complement the present study of the accuracy (defined as the agreement with the reference standard). A precision-focused study is currently underway in our research group;

(ii) Hardware development, which can include a purpose-made flexible arm with 3 translational and at least 2 rotational degrees of freedom that would enable orienting and positioning the sensor at the breast of a standing patient. The ability to image an uncompressed breast using Portable NMR would not only enable a more direct comparison between Portable NMR and reference MRI data, but also reduce the uncertainty due to variability of the degree of compression. This, in turn, can be expected to improve both the accuracy and reproducibility of Portable NMR measurements. Continued development of

Portable-NMR instrumentation with 3D imaging capabilities [78] could also be of significant advantage to biomedical applications;

(iii) Closely aligned with item (ii) is the development of quantitative, geodesic approaches to accurate topographical positioning of the Portable NMR sensor, as well as matching the physical position of the sensor to reference MR images. This would reduce the uncertainty concerning the location of the profile line in reference images. More importantly, it would enable a more reproducible and accurate positioning of the Portable NMR sensor in repeat measurements required in dynamic MD monitoring applications;

(iv) Further development of the NMR physics of the measurement methodology: Work in this direction can potentially increase the signal-to-noise ratio (SNR) achieved per unit time, as well as improve the understanding of quantitative limitations of NMR measurements in a non-uniform magnetic field. It can include exploration of different measurement modalities (e.g. CPMG vs diffusion-based measurements); numerical simulations aimed at understanding the inherent distortions introduced by a non-uniform magnetic field; development of ultrafast NMR measurement techniques specific to Portable NMR; or a direct measurement of power deposition (SAR) in Portable NMR;

(v) Specific to breast imaging applications, an investigation of different choices of topographical locations for Portable NMR scanning appears worthwhile. While the present study was limited to scanning the upper-outer quadrant of the breast, the optimal choice of the location may potentially be application-specific and could involve other regions of the breast.

The overall goal of the future work outlined above would be two-fold: to maximise the geometrical accuracy and reliability of Portable NMR measurements of the breast, and to increase the acquisition speed of Portable NMR scans in order to maximise its compatibility with the clinical workflow in prospective medical-imaging applications. Due to its low cost, low maintenance requirements and portability, single-sided Portable NMR appears an attractive technique in the context of imaging applications that do not require a millimetre-scale resolution. We hypothesise that with the appropriate development of the measurement methodology, Portable NMR can eventually become a routine tool in the medical imaging arsenal.

5. CONCLUSIONS

This work demonstrates the in-principle feasibility of using single-sided Portable NMR for spatially resolved quantification of MD-equivalent breast density *in vivo*. The approach presented is based on the measurement of the relative amplitudes of the Fat and Water components of the NMR signal acquired from the breast tissue. Earlier studies on breast tissue explants *in vitro* have demonstrated that the relative percentage of water measured using Portable NMR can be considered a MD-equivalent quantity that agrees with the reference standard (micro-CT) to within 5-10 percentage points. The agreement seen in the present study is somewhat inferior to that: the mean similarity index between Portable NMR and back-reconstructed Dixon MRI depth profiles is 0.81, corresponding to an average 19 percentage point difference between the two techniques. The decreased agreement *in vivo*, compared to studies *in vitro*, can be attributed to morphological complexity of breast tissue combined with uncertainties in the topographical positioning of Portable NMR sensor and differences in the compression of the breast in the two measurements (compressed in Portable NMR, uncompressed in 3T MRI). While this limits the currently achievable match between Portable NMR and MRI-reconstructed depth profiles, a number of avenues for the improvement of the current Portable NMR protocol are apparent. Further Portable NMR technique development, combined with the development of more sophisticated reference imaging approaches, has the potential to make Portable NMR-based assessment of Mammographic Density viable in the clinical context.

To our knowledge, the present study represents the second structured human clinical trial involving Portable NMR and the first-ever application of Portable NMR to breast imaging *in vivo*. As a low-cost, mobile, and non-ionising imaging technique, Portable NMR appears a promising modality for compositional imaging of breast and other soft tissues in the clinical context. This calls for further development of Portable NMR-based imaging *in vivo* (including further development of the physics of Portable NMR) for prospective clinical applications beyond breast imaging.

REFERENCES

[1]   Huo CW, Chew G, Hill P, Huang DX, Ingman W, Hodson L, et al. High mammographic density is associated with an increase in stromal collagen and immune cells within the mammary epithelium. Breast Cancer Res 2015;17:art. 79.

[2]   Lin SJ, Cawson J, Hill P, Haviv I, Jenkins M, Hopper JL, et al. Image-guided sampling reveals increased stroma and lower glandular complexity in mammographically dense breast tissue. Breast Cancer Research and Treatment 2011;128(2):505-16.

[3]   Huo CW, Chew GL, Britt KL, Ingman WV, Henderson MA, Hopper JL, et al. Mammographic density-a review on the current understanding of its association with breast cancer. Breast Cancer Research and Treatment 2014;144(3):479-502.

[4]   Britt KL, Ingman WV, Huo CW, Chew GL, Thompson EW. The Pathobiology of Mammographic Density. Journal of Cancer Biology & Research 2014;2(1):1021.

[5]   Tagliafico A, Bignotti B, Tagliafico G, Astengo D, Martino L, Airaldi S, et al. Breast Density Assessment Using a 3T MRI System: Comparison among Different Sequences. PLoS One 2014;9(6):e99027.

[6]   Wengert GJ, Pinker K, Helbich TH, Vogl W-D, Spijker SM, Bickel H, et al. Accuracy of fully automated, quantitative, volumetric measurement of the amount of fibroglandular breast tissue using MRI: correlation with anthropomorphic breast phantoms. NMR Biomed 2017;30:e3705.

[7]   Henze Bancroft LC, Strigel RM, Macdonald EB, Longhurst C, Johnson J, Hernando D, et al. Proton density water fraction as a reproducible MR-based measurement of breast density. Magn Reson Med 2022;87(4):1742-57.

[8]   Blend R, Rideout D, Kaizer L, Shannon P, Tudor-Robers B, Boyd N. Parenchymal patterns of the breast defined by real time ultrasound. Eur J Cancer Prev 1995;4(4):293-8.

[9]   Glide C, Duric N, Littrup P. Novel approach to evaluating breast density utilizing ultrasound tomography. Medical Physics 2007;34(2):744-53.

[10]   Maskarinec G, Morimoto Y, Laguana MB, Novotny R, Leon Guerrero RT. Bioimpedence to Assess Breast Density as a Risk Factor for Breast Cancer in Adult Women and Adolescent Girls. Asian Pacific journal of cancer prevention: APJCP 2016;17(1):65-71.

[11]   Simick MK, Jong R, Wilson B, Lilge L. Non-ionizing near-infrared radiation transillumination spectroscopy for breast tissue density and assessment of breast cancer risk. J Biomed Opt 2004;9(4):794-803.

[12]   Simick MK, Lilge L. Optical transillumination spectroscopy to quantify parenchymal tissue density: an indicator for breast cancer risk. Br J Radiol 2005;78(935):1009-17.

[13]   Hugo HJ, Tourell MC, O'Gorman PM, Paige AE, Wellard RM, Lloyd T, et al. Looking beyond the mammogram to assess mammographic density: a narrative review Biomedical Spectroscopy and Imaging 2018;7:63–80.

[14]   Houssami NL, Sarah J; Ciatto, Stefano. Breast cancer screening: emerging role of new imaging techniques as adjuncts to mammography. Med J Aust 2009;190(9):493-8.

[15]   McCormack VA, Silva IDS. Breast density and parenchymal patterns as markers of breast cancer risk: A meta-analysis. Cancer Epidemiol Biomarkers Prev 2006;15(6):1159-69.

[16]   McDonald ES, Schopp JG, Peacock S, DeMartini WD, Rahbar H, Lehman CD, et al. Diffusion-Weighted MRI: Association Between Patient Characteristics and Apparent Diffusion Coefficients of Normal Breast Fibroglandular Tissue at 3 T. Am J Roentgenol 2014;202(5):W496-W502.

[17]   Khazen M, Warren RML, Boggis CRM, Bryant EC, Reed S, Warsi I, et al. A pilot study of compositional analysis of the breast and estimation of breast mammographic density using three-dimensional T-1-weighted magnetic resonance imaging. Cancer Epidemiol Biomarkers Prev 2008;17(9):2268-74.

[18]   Dixon WT. Simple proton spectroscopic imaging. Radiology 1984;153(1):189-94.

[19]   Dixon WT. Tissue Water and Lipids: Chemical Shift Imaging and Other Methods. In: Grant DM, Harris RK, editors. Encyclopedia of Nuclear Magnetic Resonance. New York: Wiley; 1996. p. 4784-8.

[20]   Petridou E, Kibiro M, Gladwell C, Malcolm P, Toms A, Juette A, et al. Breast fat volume measurement using wide-bore 3 T MRI: comparison of traditional mammographic density evaluation with MRI density measurements using automatic segmentation. Clin Radiol 2017;72(7):565-72.

[21]   Klifa C, Carballido-Gamio J, Wilmes L, Laprie A, Shepherd J, Gibbs J, et al. Magnetic resonance imaging for secondary assessment of breast density in a high-risk cohort. Magn Reson Imaging 2010;28(1):8-15.

[22]   Wei J, Chan HP, Helvie MA, Roubidoux MA, Sahiner B, Hadjiiski LM, et al. Correlation between mammographic density and volumetric fibroglandular tissue estimated on breast MR images. Medical Physics 2004;31(4):933-42.

[23]   Wu SD, Weinstein SP, Conant EF, Kontos D. Automated fibroglandular tissue segmentation and volumetric density estimation in breast MRI using an atlas-aided fuzzy C-means method. Medical Physics 2013;40(12):122302.

[24]   Nie K, Chen JH, Chan S, Chau MKI, Yu HJ, Bahri S, et al. Development of a quantitative method for analysis of breast density based on three-dimensional breast MRI. Medical Physics 2008;35(12):5253-62.

[25]   Wang J, Azziz A, Fan B, Malkov S, Klifa C, Newitt D, et al. Agreement of Mammographic Measures of Volumetric Breast Density to MRI. PLoS One 2013;8(12):e81653.

[26]   Blumich B, Blumler P, Eidmann G, Guthausen A, Haken R, Schmitz U, et al. The NMR-mouse: Construction, excitation, and applications. Magn Reson Imaging 1998;16(5-6):479-84.

[27]   Eidmann G, Savelsberg R, Blumler P, Blumich B. The NMR MOUSE, a mobile universal surface explorer. J Magn Reson A 1996;122(1):104-9.

[28]   Blumich B, Perlo J, Casanova F. Mobile single-sided NMR. Prog Nucl Magn Reson Spectrosc 2008;52(4):197-269.

[29]   Navon G, Eliav U, Demco DE, Bluemich B. Study of order and dynamic processes in tendon by NMR and MRI. J Magn Reson Imaging 2007;25(2):362-80.

[30]   Van Landeghem M, Danieli E, Perlo J, Bluemich B, Casanova F. Low-gradient single-sided NMR sensor for one-shot profiling of human skin. J Magn Reson 2012;215:74-84.

[31]   Bergman E, Sarda Y, Ritz N, Sabo E, Navon G, Bergman R, et al. In vivo assessment of aged human skin with a unilateral NMR scanner. NMR Biomed 2015;28(6):656-66.

[32]   Roessler E, Mattea C, Stapf S. Feasibility of high-resolution one-dimensional relaxation imaging at low magnetic field using a single-sided NMR scanner applied to articular cartilage. J Magn Reson 2015;251:43-51.

[33]   Rössler E, Mattea C, Saarakkala S, Lehenkari P, Finnilä M, Rieppo L, et al. Correlations of low-field NMR and variable-field NMR parameters with osteoarthritis in human articular cartilage under load. NMR Biomed 2017;30(8):e3738.

[34]   Brizi L, Barbieri M, Baruffaldi F, Bortolotti V, Fersini C, Liu H, et al. Bone volume–to–total volume ratio measured in trabecular bone by single-sided NMR devices. Magn Reson Med 2018;79(1):501-10.

[35]   Barbieri M, Fantazzini P, Testa C, Bortolotti V, Baruffaldi F, Kogan F, et al. Characterization of Structural Bone Properties through Portable Single-Sided NMR Devices: State of the Art and Future Perspectives. Int J Mol Sci 2021;22(14):art. 07318.

[36]   Barbieri M, Fantazzini P, Bortolotti V, Baruffaldi F, Festa A, Manners DN, et al. Single-sided NMR to estimate morphological parameters of the trabecular bone structure. Magn Reson Med 2021;85(6):3353-69.

[37]   Sarda Y, Bergman E, Hillel I, Binderman I, Nevo U. Detection of bone marrow changes related to estrogen withdrawal in rats with a tabletop stray-field NMR scanner. Magn Reson Med 2017;78(3):860-70.

[38]   Keschenau PR, Klingel H, Reuter S, Foldenauer AC, Viess J, Weidener D, et al. Evaluation of the NMR-MOUSE as a new method for continuous functional monitoring of the small intestine during different perfusion states in a porcine model. PLoS One 2018;13(11):e0206697.

[39]   Keschenau PR, Simons N, Klingel H, Reuter S, Foldenauer AC, Viess J, et al. Perfusion-related changes in intestinal diffusion detected by NMR-MOUSE (R) monitoring in minipigs. Microvasc Res 2019;125:103876.

[40]   McDaniel PC, Cooley CZ, Stockmann JP, Wald LL. The MR Cap: A single-sided MRI system designed for potential point-of-care limited field-of-view brain imaging. Magn Reson Med 2019;82(5):1946-60.

[41]   Bashyam A, Frangieh CJ, Li M, Cima MJ. Dehydration assessment via a portable, single sided magnetic resonance sensor. Magn Reson Med 2020;83(4):1390-404.

[42]   Morris RH, Almazrouei NK, Trabi CL, Newton MI. NMR CAPIBarA: Proof of Principle of a Low-Field Unilateral Magnetic Resonance System for Monitoring of the Placenta during Pregnancy. Appl Sci-Basel 2020;10(1):art. 162.

[43]   Williamson NH, Ravin R, Cai TX, Benjamini D, Falgairolle M, O'Donovan MJ, et al. Real-time measurement of diffusion exchange rate in biological tissue. J Magn Reson 2020;317:106782.

[44]   Bashyam A, Frangieh CJ, Raigani S, Sogo J, Bronson RT, Uygun K, et al. A portable single-sided magnetic-resonance sensor for the grading of liver steatosis and fibrosis. Nature Biomedical Engineering 2021;5(3):240-51.

[45]   Cooley CZ, McDaniel PC, Stockmann JP, Srinivas SA, Cauley SF, Śliwiak M, et al. A portable scanner for magnetic resonance imaging of the brain. Nature biomedical engineering 2021;5(3):229-39.

[46]   Thomas DG, Galvosas P, Tzeng YC, Harrison FG, Berry MJ, Teal PD, et al. Oxygen saturation-dependent effects on blood transverse relaxation at low fields. Magn Reson Mat Phys Biol Med 2022:in press.

[47]   Tourell MC, Ali TS, Hugo HJ, Pyke C, Yang S, Lloyd T, et al. T1-based sensing of mammographic density using single-sided portable NMR Magn Reson Med 2018;80:1243-51.

[48]   Ali TS, Tourell MC, Hugo HJ, Pyke C, Yang S, Lloyd T, et al. Transverse relaxation-based assessment of mammographic density and breast tissue composition by single-sided portable NMR. Magn Reson Med 2019;82(3):1199-213.

[49]   Huang X, Ali TS, Nano T, Blick T, Tse BW-C, Sokolowski K, et al. Quantification of breast tissue density: Correlation between single-sided portable NMR and micro-CT measurements. Magn Reson Imaging 2019;62:111-20.

[50]   Alqurashi M, Momot KI, Aamry A, Almohammed HI, Aamri H, Johary YH, et al. Sensing Mammographic Density using single-sided portable Nuclear Magnetic Resonance. Saudi Journal of Biological Sciences 2022;29(4):2447-54.

[51]   Huang X, Reye G, Momot KI, Blick T, Lloyd T, Tilley WD, et al. Heparanase Promotes Syndecan-1 Expression to Mediate Fibrillar Collagen and Mammographic Density in Human Breast Tissue Culturedex vivo. Front Cell Dev Biol 2020;8:art. 599.

[52]   Miltner O, Schwaiger A, Schmidt C, Bucker A, Kolker C, Siebert CH, et al. Portable NMR-MOUSE (R): a new method and its evaluation of the Achilles tendon. Z Orthop Grenzg 2003;141(2):148-52.

[53]   Van Landeghem M, Bresson B, Blumich B, de Lacaillerie JBD. Micrometer scale resolution of materials by stray-field Magnetic Resonance Imaging. J Magn Reson 2011;211(1):60-6.

[54]   Colucci LA, Corapi KM, Li M, Parada XV, Allegretti AS, Lin HY, et al. Fluid assessment in dialysis patients by point-of-care magnetic relaxometry. Sci Transl Med 2019;11(502):eaau1749.

[55]   Bland JM, Altman DG. Statistical methods for assessing agreement between two methods of clinical measurement. Lancet 1986;1(8476):307-10.

[56]   Danieli E, Bluemich B. Single-sided magnetic resonance profiling in biological and materials science. J Magn Reson 2013;229:142-54.

[57]   Venkataramanan L, Song YQ, Hurlimann MD. Solving Fredholm integrals of the first kind with tensor product structure in 2 and 2.5 dimensions. IEEE Trans Signal Process 2002;50(5):1017-26.

[58]   Boyd NF, Guo H, Martin LJ, Sun L, Stone J, Fishell E, et al. Mammographic Density and the Risk and Detection of Breast Cancer. N Engl J Med 2007;356(3):227-36.

[59] Huo CW, Waltham M, Khoo C, Fox SB, Hill P, Chen S, et al. Mammographically dense human breast tissue stimulates MCF10DCIS.com progression to invasive lesions and metastasis. Breast Cancer Res 2016;18:106.

[60] Wolfe JN. Breast patterns as an index of risk for developing breast cancer. Am J Roentgenol 1976;126(6):1130-7.

[61] Yaffe MJ. Mammographic density. Measurement of mammographic density. Breast Cancer Research: BCR 2008;10(3):art. 209.

[62] Bond-Smith D, Stone J. Methodological Challenges and Updated Findings from a Meta-analysis of the Association between Mammographic Density and Breast Cancer. Cancer Epidemiol Biomarkers Prev 2019;28(1):22-31.

[63] Carney PA, Miglioretti DL, Yankaskas BC, Kerlikowske K, Rosenberg R, Rutter CM, et al. Individual and combined effects of age, breast density, and hormone replacement therapy use on the accuracy of screening mammography. Ann Intern Med 2003;138(3):168-75.

[64] Buist DSM, Porter PL, Lehman C, Taplin SH, White E. Factors Contributing to Mammography Failure in Women Aged 40–49 Years. J Natl Cancer Inst 2004;96(19):1432-40.

[65] Yaghjyan L, Colditz GA, Collins LC, Schnitt SJ, Rosner B, Vachon C, et al. Mammographic Breast Density and Subsequent Risk of Breast Cancer in Postmenopausal Women According to Tumor Characteristics. J Natl Cancer Inst 2011;103(15):1179-89.

[66] Nickel B, Farber R, Brennan M, Hersch J, McCaffery K, Houssami N. Breast density notification: evidence on whether benefit outweighs harm is required to inform future screening practice. BMJ Evid Based Med 2021;26(6):309-11.

[67] Nickel B, Copp T, Brennan M, Farber R, McCaffery K, Houssami N. The Impact of Breast Density Information or Notification on Women's Cognitive, Psychological, and Behavioral Outcomes: A Systematic Review. J Natl Cancer Inst 2021;113(10):1299-328.

[68] Dench EK, Darcey EC, Keogh L, McLean K, Pirikahu S, Saunders C, et al. Confusion and Anxiety Following Breast Density Notification: Fact or Fiction? J Clin Med 2020;9(4):art. 955.

[69] Shawky M, Martin H, Hugo H, Lloyd T, Britt K, Redfern A, et al. Mammographic density: a potential monitoring biomarker for adjuvant and preventative breast cancer endocrine therapies. Oncotarget 2017;8(3):5578-91.

[70] Mullooly M, Pfeiffer RM, Nyante SJ, Heckman-Stoddard BM, Perloff M, Jatoi I, et al. Mammographic Density as a Biosensor of Tamoxifen Effectiveness in Adjuvant Endocrine Treatment of Breast Cancer: Opportunities and Implications. J Clin Oncol 2016;34(18):2093-7.

[71] Elsamany S, Alzahrani A, Abozeed WN, Rasmy A, Farooq MU, Elbiomy MA, et al. Mammographic breast density: Predictive value for pathological response to neoadjuvant chemotherapy in breast cancer patients. Breast (Edinburgh, Scotland) 2015;24(5):576-81.

[72] Chistiakov DA, Voronova NV, Chistiakov PA. Genetic variations in DNA repair genes, radiosensitivity to cancer and susceptibility to acute tissue reactions in radiotherapy-treated cancer patients. Acta Oncol 2008;47(5):809-24.

[73]   de Visser SK, Bowden JC, Wentrup-Byrne E, Rintoul L, Bostrom T, Pope JM, et al. Anisotropy of collagen fibre alignment in bovine cartilage: Comparison of polarised light microscopy and spatially-resolved diffusion-tensor measurements. Osteoarthr Cartilage 2008;16(6):689-97.

[74]   Bottomley PA, Edelstein WA. Power deposition in whole-body NMR imaging. Medical Physics 1981;8(4):510-2.

[75]   Faes TJC, van der Meij HA, de Munck JC, Heethaar RM. The electric resistivity of human tissues (100 Hz-10 MHz): a meta-analysis of review studies. Physiological Measurement 1999;20(4):R1-R10.

[76]   Bottomley PA, Redington RW, Edelstein WA, Schenck JF. Estimating radiofrequency power deposition in body NMR imaging Magn Reson Med 1985;2(4):336-49.

[77]   International Commission on Non-Ionizing Radiation Protection. Guidelines for Limiting Exposure to Electromagnetic Fields (100 kHz to 300 GHz). Health Physics 2020;118(5):483-524.

[78]   Casanova F, Blumich B. Two-dimensional imaging with a single-sided NMR probe. J Magn Reson 2003;163(1):38-45.

Table captions

Table 1: Profile similarity indices (SI) for the three comparison pairs: Portable NMR - Dixon, Portable NMR - T_1, and Dixon - T_1. The profile-average and breast-average water fractions WF (as measured from the Dixon data) are shown for each participant for reference.

Participant	BI-RADS category	Average WF over entire right breast (Dixon)	Average WF over profile line (Dixon)	SI		
				pNMR-Dixon	pNMR-T_1	Dixon-T_1
1	c	0.148	0.416	0.789	0.812	0.783
2	c	0.111	0.243	0.904	0.863	0.922
3	c	0.089	0.302	0.873	0.819	0.864
4	c	0.064	0.168	0.869	0.861	0.964
5	d	0.133	0.489	0.648	0.684	0.907
6	c	0.071	0.204	0.888	0.845	0.919
7	c	0.098	0.312	0.856	0.876	0.911
8	d	0.191	0.425	0.820	0.807	0.876
9	d	0.378	0.536	0.832	0.821	0.669
10	b	0.067	0.153	0.849	0.852	0.951
11	d	0.100	0.289	0.890	0.830	0.922
12	c	0.137	0.208	0.848	0.803	0.944
13	b	0.095	0.308	0.681	0.716	0.881
14	d	0.224	0.489	0.742	0.737	0.909
15	c	0.084	0.360	0.728	0.821	0.871

Table 2: Bland-Altman parameters for the three comparison pairs: Portable NMR - Dixon, Portable NMR - T_1, and Dixon - T_1. The quantity compared is the water fraction WF (physical range from 0 to 1). For each pair, a negative value of the Mean indicates that the first technique in the pair underestimates WF compared to the second technique. "Mean-abs" signifies that the Average-over-Cohort values of the Mean represent averaging of the absolute values, not the signed quantities.

Participant	pNMR-Dixon		pNMR-T_1		Dixon-T_1	
	Mean	σ	Mean	σ	Mean	σ
1	-0.130	0.236	0.023	0.220	0.154	0.201
2	0.030	0.139	-0.006	0.234	-0.036	0.163
3	-0.065	0.155	-0.126	0.161	-0.061	0.185
4	-0.114	0.118	-0.122	0.095	-0.008	0.044
5	-0.343	0.216	-0.316	0.190	0.028	0.131
6	-0.066	0.112	-0.122	0.129	-0.056	0.139
7	-0.039	0.155	-0.053	0.153	-0.013	0.117
8	0.012	0.235	-0.087	0.237	-0.099	0.117
9	-0.033	0.275	-0.130	0.194	-0.097	0.394
10	-0.130	0.082	-0.148	0.030	-0.018	0.093
11	0.023	0.135	0.093	0.184	0.070	0.099
12	0.056	0.175	0.029	0.226	-0.027	0.109
13	-0.195	0.311	-0.196	0.256	-0.002	0.190
14	0.135	0.327	0.064	0.300	-0.071	0.139
15	-0.272	0.243	-0.179	0.089	0.093	0.218
Average over cohort	**0.11** (mean-abs)	**0.19**	**0.11** (mean-abs)	**0.18**	**0.06** (mean-abs)	**0.16**

Figure captions

Figure 1: Portable NMR measurements: (a) A schematic diagram of the Portable NMR instrument (NMR-MOUSE PM25). $\mathbf{B}_0$, the vector of the static magnetic field; $\mathbf{g}$, the vector of the magnetic field gradient; the red line and circle show the sensing slice; (b) The setup of Portable NMR breast measurements *in vivo*. The upper-outer quadrant of the participant's right breast presses against the top stage of the Portable NMR instrument. The depth of the sensing slice is controlled by moving the lift in the vertical direction (*z* axis) while the participant's breast is stationary on the sample stage. The topmost position of the sensor (pressed against the skin) corresponded to the maximum measurement depth (20.8 mm), while measurement at the skin surface corresponded to the sensor being 20.8 mm below the skin surface.

Figure 2: Reconstruction of the 1D depth profile from 3T MR images: (a) The location of the centre of the sensor coil was identified by comparing the topographical features of the breast in MR images with the photograph showing the position marker (yellow dot); (b) In 3T MR images, Portable NMR sensing slices were identified as 100 μm thick curved slabs (red lines) parallel to the skin surface (yellow line). These slices become flat when the breast is compressed against the Portable NMR sensor. The blue line is the normal to the skin surface passing through the centre of the Portable NMR sensor.

Figure 3: Illustration of the physical meaning of the similarity index SI, Eq. (4). The value of SI is the ratio of the area between the two curves (shaded area *A*) to the area of the entire plot (the dashed rectangle *R*). The entire shaded area is taken with the positive sign, i.e., the index is sensitive to the absolute distance between the two curves but not to the sign of the difference. The value of (1 - SI) represents the mean absolute difference between the two curves, normalised to the size of the physical range of the quantity measured. The value of SI can range between 0 (when one curve has the constant value of 1 while the other has the value of 0) and 1 (the two curves are identical). In the example shown SI = 0.88, which corresponds to a 12 percentage point mean absolute-value difference between the two curves.

Figure 4: Representative Portable NMR data: (a) The primary dataset is a Carr-Purcell-Meiboom-Gill (CPMG) decay; (b) The T_2 relaxation spectrum is obtained by an inverse Laplace transform (ILT) of the CPMG decay. The two major peaks in (b) correspond to the two chemical components contributing to Portable NMR signal: water (left) and fat (right). The relative areas of the two peaks represent the relative amounts of the two components, and by inference the amounts of FGT and adipose tissue. The data shown is from participant 11, tissue depth 16.8 mm.

Figure 5: Representative Dixon MR images: (a) Primary image with the water and fat signals in-phase; (b) Primary image with the water and fat signals 180º out-of-phase; (c) Reconstructed water-only image; (d) Reconstructed fat-only image. The images shown are from the same participant as in Fig. 4. All four images are shown on the same intensity scale. The red line in (a) indicates the approximate location of the Portable-NMR sensing slice corresponding to Fig. 4. The red arrow shows the approximate positioning of the Portable NMR sensor.

Figure 6: Representative T_1-weighted MR images: (a) TI = 210 ms (fat-suppressed); (b) TI = 690 ms (water-suppressed); (c) TI = 3000 ms ("full-intensity"). The images shown are from the same participant as in Fig. 4. All three images are shown on the same intensity scale. The red line in (c) indicates the approximate location of the Portable-NMR sensing slice corresponding to Fig. 4. The red arrow shows the approximate positioning of the Portable NMR sensor.

Figure 7: Representative depth profiles of tissue water fraction [WF, Eq. (3)]: (a) Example of a good agreement between Portable NMR and 3T MRI (participant 11); (b) Example of a poor agreement (participant 14). Notation is as follows: ●, profile directly measured using Portable NMR; ●, profile reconstructed from Dixon MRI data; ●, profile reconstructed from T_1-weighted MRI data.

SUPPLEMENTARY MATERIAL FOR:

Portable NMR for quantification of breast density *in vivo*:
Proof-of-concept measurements and comparison with quantitative MRI

Nicholas D. McKay-Parry[^,1], Tony Blick[^,2, 3], Satcha Foongkajornkiat[4], Thomas Lloyd[5],

Erik W. Thompson[2,3], Honor J. Hugo[2,3,6,7] and Konstantin I. Momot[4]*

[1] Department of Medical Imaging, Gold Coast University Hospital, Southport, QLD 4215, Australia

[2] School of Biomedical Sciences, Queensland University of Technology (QUT), Brisbane, QLD 4006, Australia

[3] Translational Research Institute, Woolloongabba, QLD 4102, Australia

[4] School of Chemistry and Physics, Queensland University of Technology (QUT), Brisbane, QLD 4001, Australia

[5] Department of Radiology, The Princess Alexandra Hospital, Woolloongabba, QLD 4102, Australia

[6] School of Health and Behavioural Sciences, University of the Sunshine Coast, Sippy Downs, QLD 4556, Australia

[7] School of Medicine and Dentistry, Griffith University, Birtinya, QLD 4575, Australia

^ = Equal first authors

* Corresponding author:
Dr. Konstantin I. Momot
School of Chemistry and Physics
Queensland University of Technology (QUT)
GPO Box 2434, QLD 4001, Brisbane, Australia
Phone: +61-7-3138-1173
Email: k.momot@qut.edu.au

1.   Derivation of Equation (1)

Equation (1) (main text, Section 2.5) represents the relative amplitude of the MR signal of chemical component i in inversion-recovery measurements as a function of the inversion-recovery period TI and recycle time TR. The equation is based on the assumption that the value of the longitudinal magnetisation immediately prior to the inversion 180° RF pulse reaches a non-equilibrium steady-state value $M_{ss} \neq M_0$ if TR has a finite duration. The value of M_{ss} can be obtained by considering the relaxation of longitudinal magnetisation $M_z(t)$ during the period TR, approximating $M_z(t)$ as unperturbed (in the time-averaged sense) by any other RF pulses during that period:

$$M_z(t) = M_0 + \left[M_z(0) - M_0\right]e^{-t/T_1} \tag{SM1}$$

where t is the time elapsed since the last 180° inversion RF pulse. Assuming that the steady state had been established and the 180° inversion RF pulse is perfect, the value of M_z immediately prior to the 180° inversion pulse is $M_z(\text{TR}) = M_{ss}$ and its value immediately after the inversion pulse is $M_z(0) = -M_{ss}$. Recasting Eq. (SM1) with these values and using $t = \text{TR}$ yields

$$M_{ss} = M_0 + \left[-M_{ss} - M_0\right]e^{-TR/T_1} \tag{SM2}$$

Solving Eq. (SM2) for M_{ss} produces

$$M_{ss} = M_0 \cdot \frac{1 - e^{-TR/T_1}}{1 + e^{-TR/T_1}} \tag{SM3}$$

To obtain the value of longitudinal magnetisation at the end of the inversion-recovery period TI, substitute $M_z(0) = -M_{ss}$ and $t = \text{TI}$ into Eq. (SM1), combining the result with Eq. (SM3):

$$M_z(TI) = M_0 + \left[-M_0 \cdot \frac{1 - e^{-TR/T_1}}{1 + e^{-TR/T_1}} - M_0\right] \cdot e^{-TI/T_1} \tag{SM4}$$

Equation (SM4) leads to

$$\frac{M_z(TI)}{M_0} = 1 - \frac{2}{1 + e^{-TR/T_1}} \cdot e^{-TI/T_1} \tag{SM5}$$

which translates into the MRI signal of the i-th chemical component given by Eq. (1) in the main text.

2.   Spatial profile of the RF field amplitude

Given a known duration of the nominal 180° RF pulse, t_{P180}, the value of the rotating-frame B_1 field can be obtained using the textbook relationship between the two:

$$B_1 = \frac{\pi}{\gamma \, t_{P90}} \tag{SM6}$$

where $\gamma = 26.75 \cdot 10^7$ rad/T·m is the gyromagnetic ratio of the ^{1}H nucleus. As the RF coil of the PM25 NMR-MOUSE instrument is a surface coil, the t_{P180} and B_1 both exhibit a strong dependence upon the distance d from the plane of the coil. Table ST1 presents this dependence for the NMR-MOUSE instrument used in the present study: the calibrated values of t_{P980}, the B_1 values calculated using Eq. (SM6) and the values of the laboratory-frame RF magnetic field $B_{RF} = 2B_1$ are shown for different values of d.

Table ST1.   Spatial profile of the calibrated duration of the nominal 180° RF pulse (t_{P180}), the calculated B_1 field and the corresponding RF field B_{RF}. The t_{P180} values were calibrated at the same RF transmit power at all locations.

d (mm)	t_{P180} (µs)	B_1 (mT)	B_{RF} (mT)
5.9	6.5	1.81	3.61
10.8	11.0	1.07	2.14
15.7	16.0	0.734	1.47
20.8	27.0	0.435	0.870
26.0	40.0	0.294	0.587

This spatial profile of B_{RF} can be extrapolated to $d = 0$ (or any other distance) by approximating the NMR-MOUSE sensor coil as an ideal loop with a circulating electric current. An ideal circular loop of radius R with an electric current I produces the magnetic field that is dependent upon the distance d from the plane of the coil. On the symmetry axis of the circular loop, the component of the magnetic field normal to the loop is given by

$$B_z(d) = \frac{\mu_0}{4\pi} \frac{2\pi R^2 I}{\left(d^2 + R^2\right)^{3/2}} \tag{SM7}$$

where $\mu_0/4\pi = 10^{-7}$ T·m/A is the magnetic permeability of free space. It is easily seen that the spatial profile of B_z can be linearised by plotting $(B_z^{-2/3})$ vs (d^2). This linearisation also enables the effective radius of the RF coil to be estimated from the relationship $R^2 = $ (Intercept)/(Slope). Figure SF1 presents such a linearised plot for the NMR-MOUSE data from Table ST1. The linear extrapolation to $d = 0$ yields an estimate of the value of B_{RF} in the centre of the sensor coil: $B_{RF0} = 3.97$ mT. This represents the highest possible value of B_{RF} at the given RF Transmit power. The square root of the (Intercept)/(Slope) ratio yields the effective coil radius, $R = 16.1$ mm.

Figure SF1. Linearised spatial profile of the amplitude of the RF magnetic field B_{RF}. The dots correspond to the values of B_{RF} given in Table ST1; the straight line represents a linear least-squares fit. The y-intercept of the line yields the value of B_{RF} in the centre of the RF coil: $B_{RF0} = 3.97$ mT. The (Intercept)/(Slope) ratio yields effective $R = 16.1$ mm. The good linearity of the fit confirms that Eq. (SM7) is a reasonable approximation for the spatial profile of the RF field.
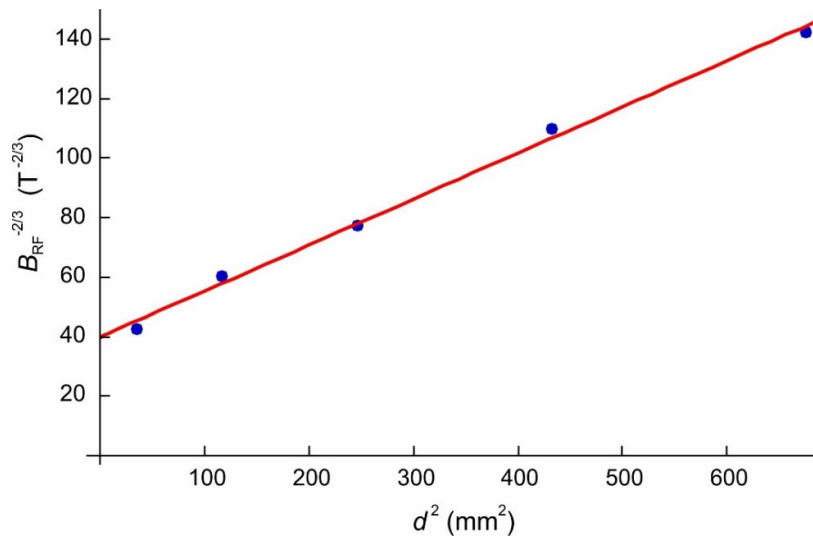
3.   Calculation of the Specific Absorption Rate (SAR)

The tissue RF power deposition during a Portable NMR CPMG measurement can be estimated using the equation adapted from ref. [74]:

$$P = \frac{\pi^2\, \nu^2\, B_{RF}^2\, R^2}{2\rho\, s}\, D \qquad\qquad (\text{SM8})$$

where $D = \text{NE} \cdot t_{P180}/\text{TR}$ is the RF duty cycle if the excitation 90° RF pulse is neglected. The resulting P represents the Specific Absorption Rate (SAR) in W/kg. For a surface coil, R has the meaning of the radius of the coil; its effective value was estimated in the previous section as 16.1 mm. The other parameters used in Eq. (SM8) are identical to those used in ref. [74]: ν, RF frequency (Hz); ρ, tissue resistivity ($\Omega \cdot$m); and s, tissue density (kg/m^3). Other factors (most notably ρ and s) being equal, the highest power deposition in a NMR-MOUSE measurement can be expected to occur in the layer of tissue immediately adjacent to the sensor coil. Therefore, using the B_{RF0} obtained above for the value of B_{RF} gives an estimate of the highest RF power deposition in any gram of tissue. Using the parameter values presented in Table ST2, Eq. (SM8) yields $P = 2.4$ W/kg.

Table ST2.   Parameter values used for the calculation of SAR in the layer of tissue immediately adjacent to the RF sensor coil. The value of SAR was calculated using Eq. (SM8), which yielded $P = 2.4$ W/kg.

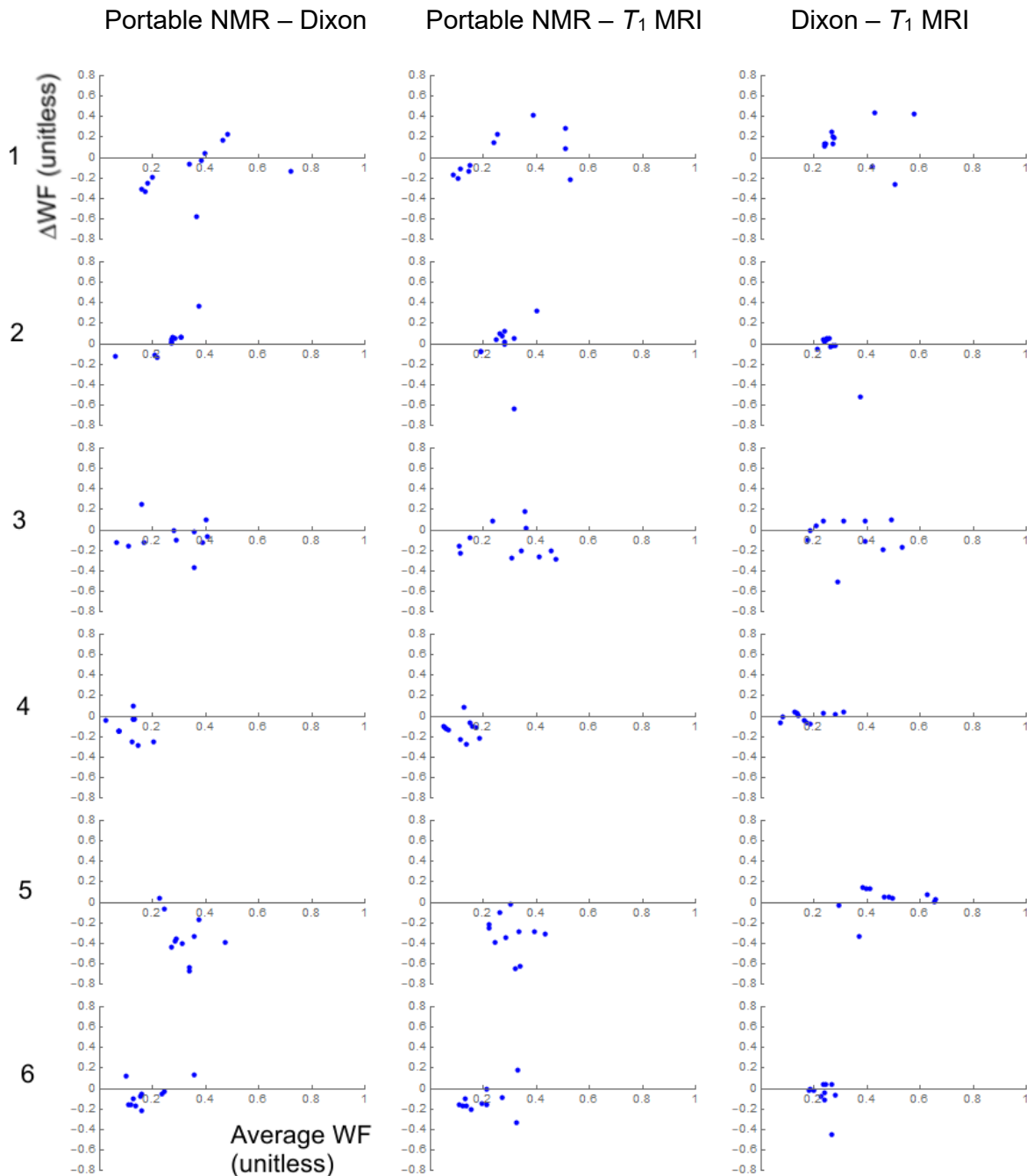| Parameter	Value	Known or estimated?
ν	$13.18 \cdot 10^6$ Hz	Known – spectrometer operating frequency
B_{RF}	$3.97 \cdot 10^{-3}$ T	Upper estimate: B_{RF0} is used as the highest-possible B_{RF}
R	$16.1 \cdot 10^{-3}$ m	Effective radius from fitting the circular-loop model
ρ	$2.0\ \Omega \cdot$m	Lower estimate for $\nu = 15$ MHz, based on ref. [75]
s	$1 \cdot 10^3$ kg/m^3	Estimated as the average density of skin, fat and FGT
NE	1000	Known – operator-set pulse sequence parameter
t_{P180}	$27 \cdot 10^{-6}$ s	Known – operator-set pulse sequence parameter
TR	20 s	Known – operator-set pulse sequence parameter

4.   Complete set of depth profiles

Figure SF2.   Depth profiles of the water fraction (WF) obtained from direct Portable NMR measurements (blue dots, ●) and reference-standard depth profiles reconstructed from Dixon 3D MRI data (red dots, ●) and from T_1-weighted 3D MRI data (green dots, ●). The numbers inside the panels represent the patient from whom the profiles were acquired.
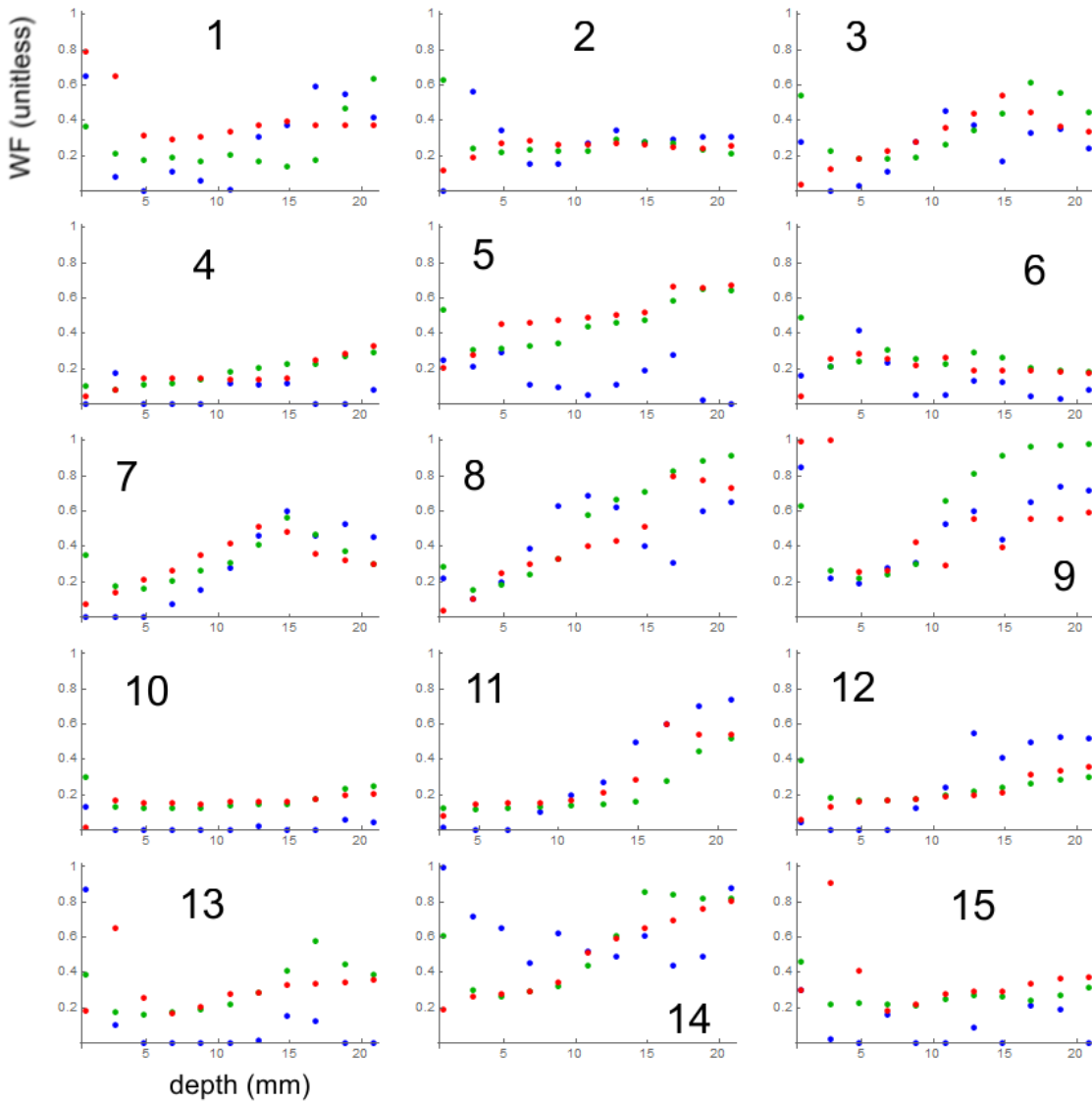
5. Bland-Altman analysis

Figure SF3. Bland-Altman plots for pairwise comparison of the sets of depth profiles obtained from direct Portable NMR measurements and reference-standard depth profiles reconstructed from Dixon 3D MRI data and from T_1-weighted 3D MRI data. The 15 numbered rows represent individual patients; the three columns correspond to the three comparison pairs.

Portable NMR – Dixon   Portable NMR – T_1 MRI   Dixon – T_1 MRI

ΔWF (unitless)

7

8

9

10

11

12

Average WF
(unitless)

Portable NMR – Dixon   Portable NMR – T_1 MRI   Dixon – T_1 MRI

ΔWF (unitless)

13

14

15

Average WF (unitless)